Supporting Information

Microwave-Assisted Synthesis of Core–Shell Structured Pd@PdPtCuFe Recessed Truncated Octahedral Nanocrystals for Multifunctional Electrocatalysis

Dezhong Hu[a], Wendan Jiang[a], Wei Keat Ng [a], Jun Yang[b,*], and Xiongwu Kang[a,*]

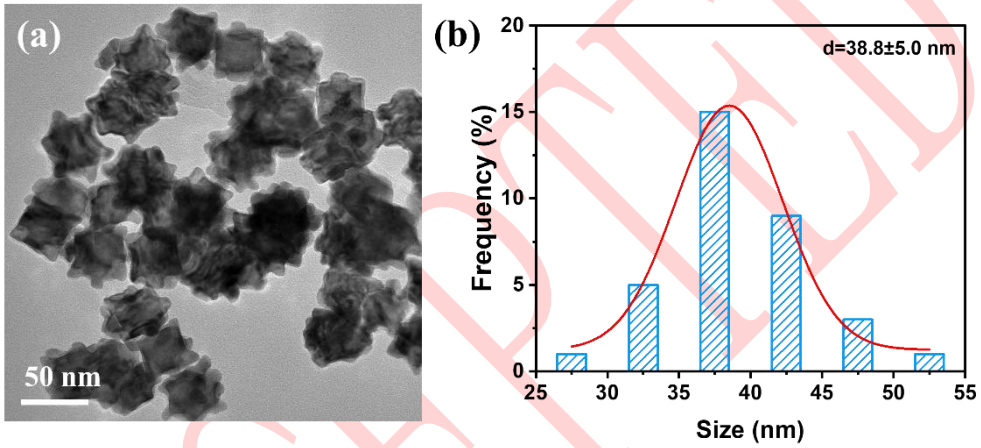

Figure S1. TEM image and particle size distribution of Pd@PdPtCuFe nanocrystals.

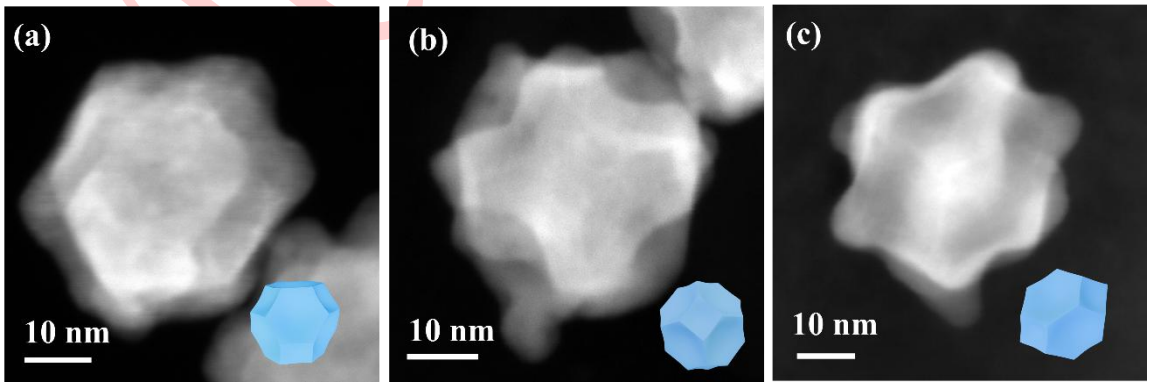

Figure S2. HAADF STEM of single Pd@PdPtCuFe nanocrystal at at different orientations.

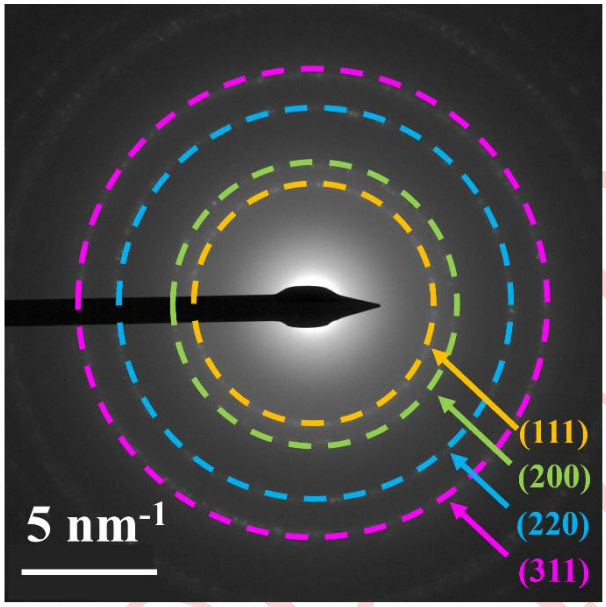

Figure S3. selected area electron diffraction (SAED) image of Pd@PdPtCuFe.

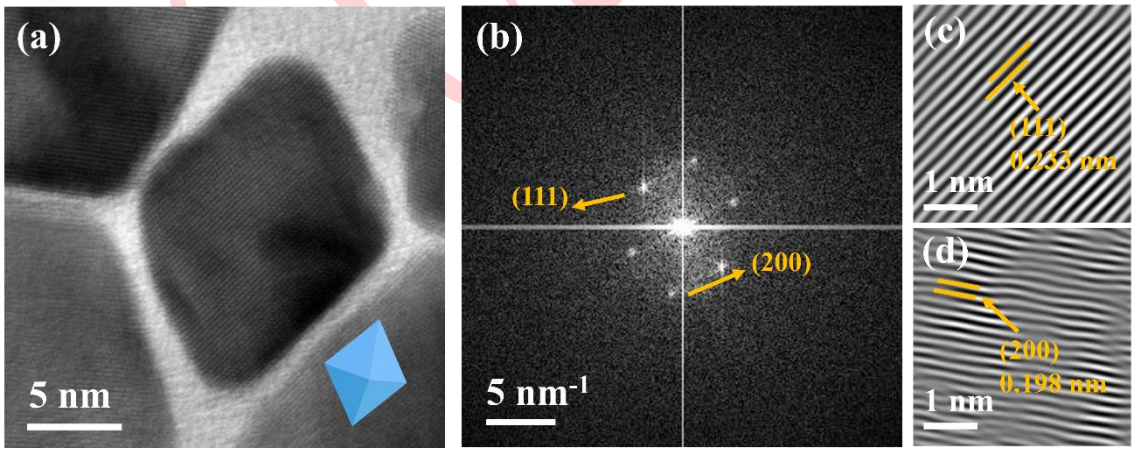

Figure S4. (a) HRTEM image, (b) FFT pattern, (c) (111) Lattice space, (d) (200) lattice space of Pd@PdPtCu.

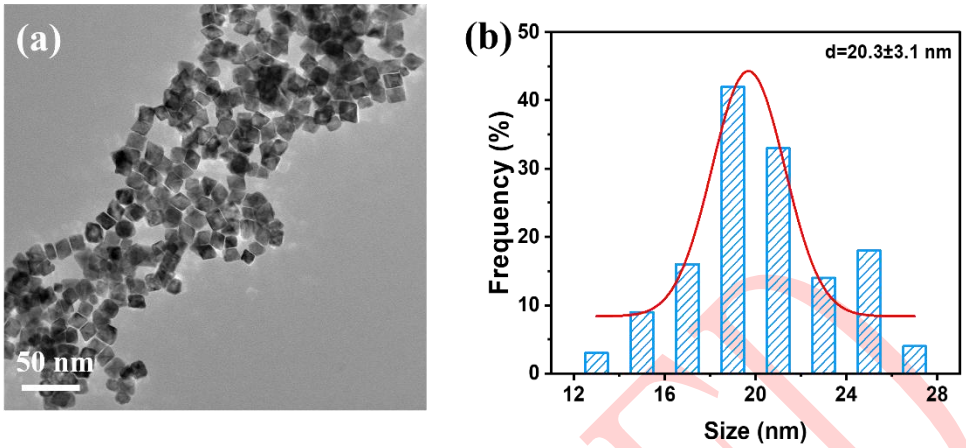

Figure S5. TEM image and particle size distribution of Pd@PdPtCu nanocrystals.

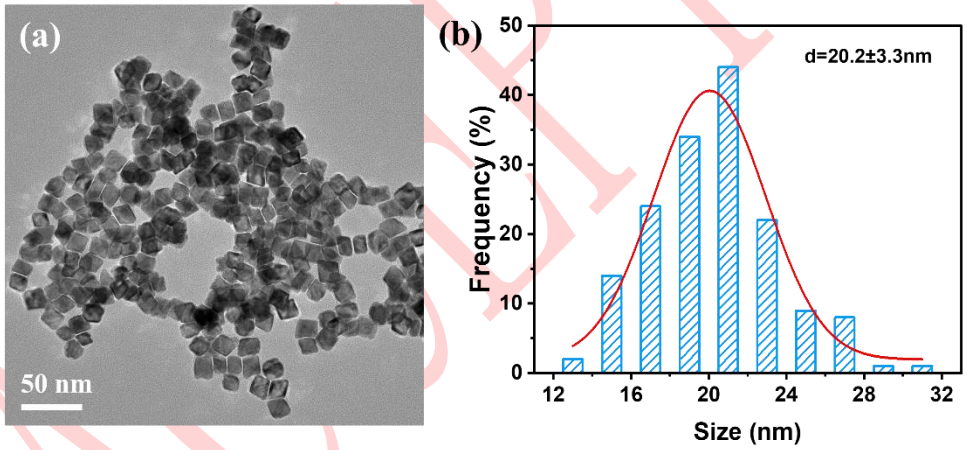

Figure S6. TEM image and particle size distribution of Pd@PdPtCuCo nanocrystals.

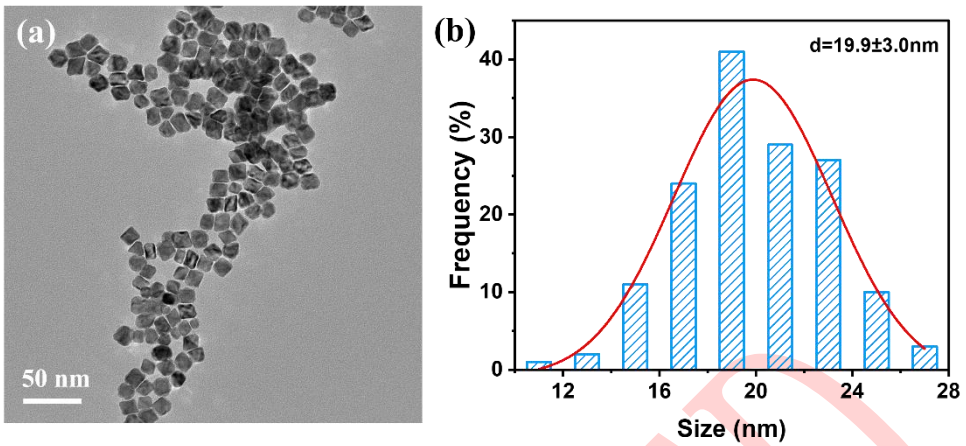

Figure S7. TEM image and particle size distribution of Pd@PdPtCuNi nanocrystals.

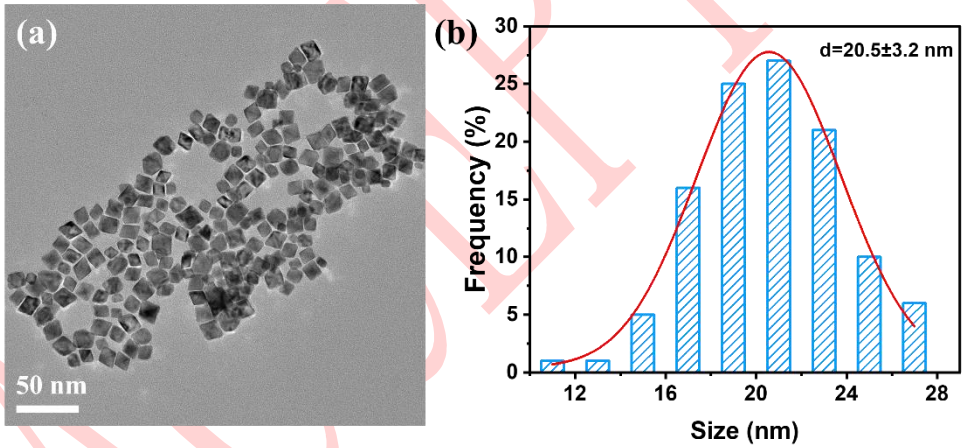

Figure S8. TEM image and particle size distribution of Pd@PdPtCuZn nanocrystals.

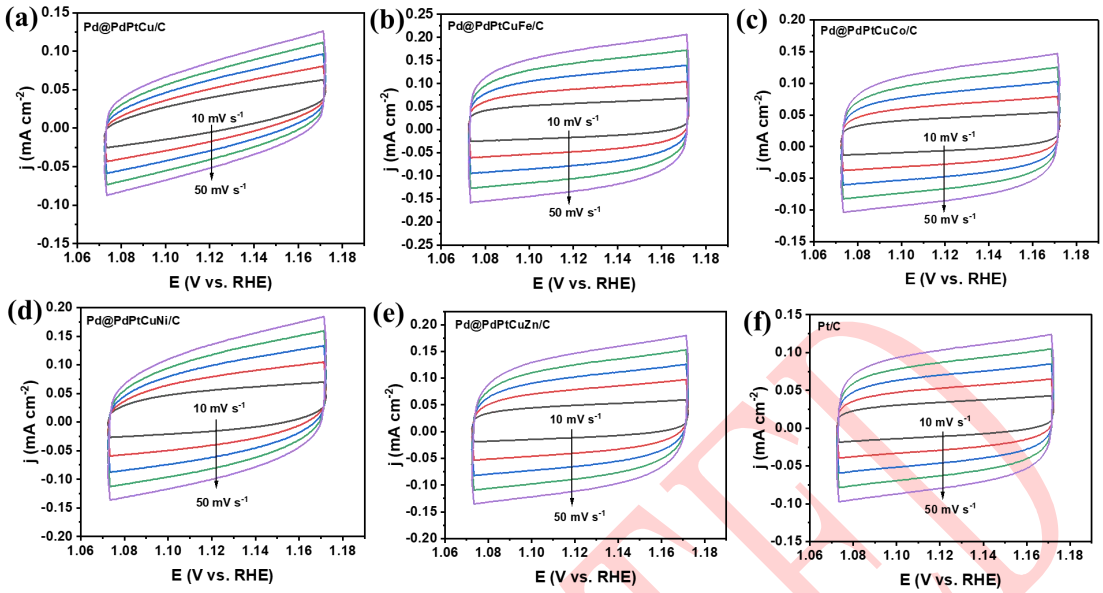

Figure S9. Cyclic voltammetry (CV) curves of catalysts recorded in 1 M KOH electrolyte at various scan rates (10–50 mV s^{-1}): (a) Pd@PdPtCu/C, (b) Pd@PdPtCuFe/C, (c) Pd@PdPtCuCo/C, (d) Pd@PdPtCuNi/C, (e) Pd@PdPtCuZn/C, and (f) Pt/C.

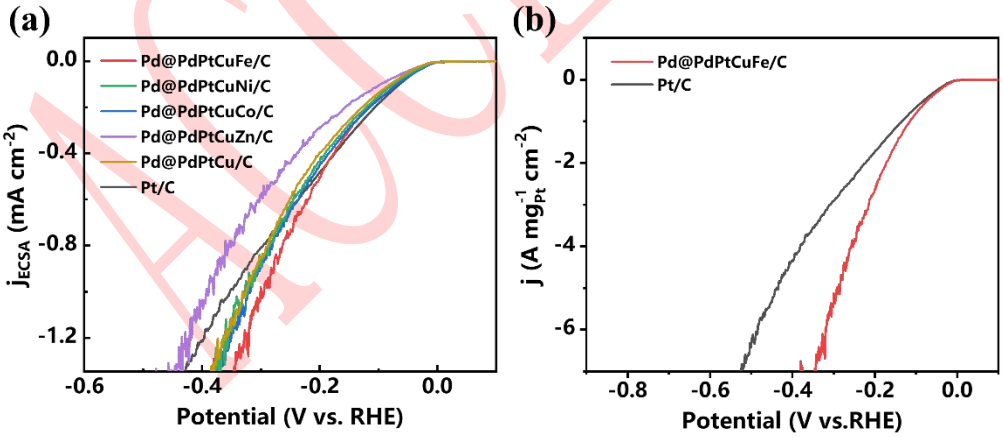

Figure S10. (a) HER polarization curves normalized to the ECSA. (b) HER polarization curves normalized to the mass activity.

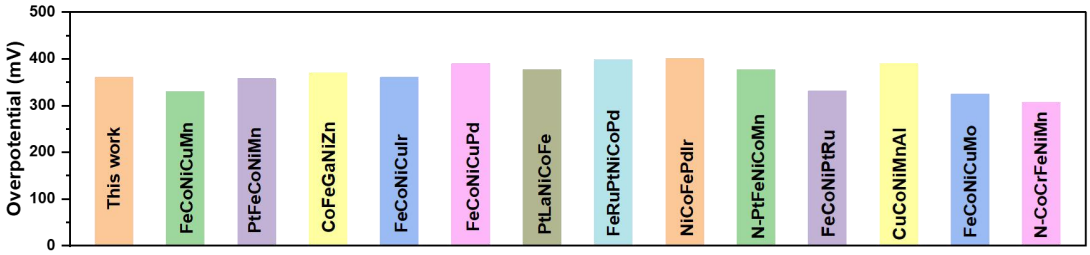

Figure S11. comparison of OER overpotentials with previously reported catalysts

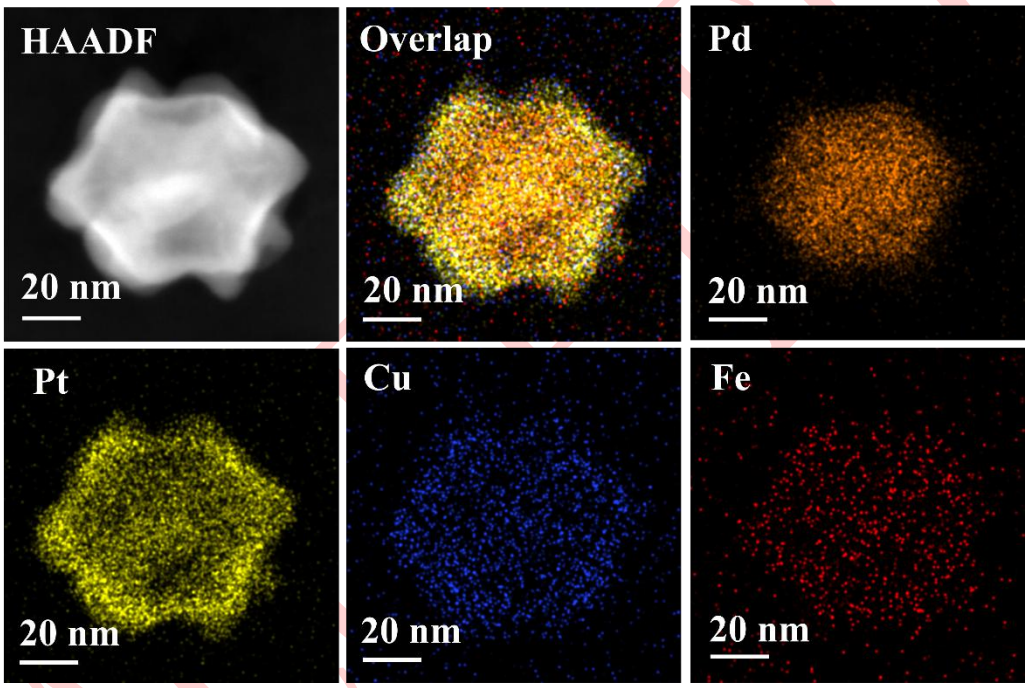

Figure S12. HAADF-STEM image and corresponding EDS image of Pd@PdPtCuFe after OER stability test.

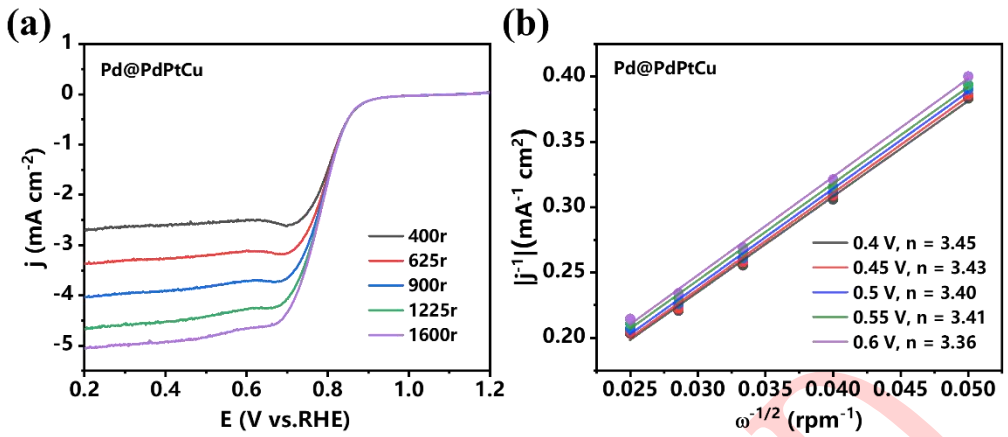

Figure S13 (a) Rotating disk voltammogram (RDV) curves at different rotation rates of Pd@PdPtCu in 0.1 M KOH electrolyte. (b) K−L plots.

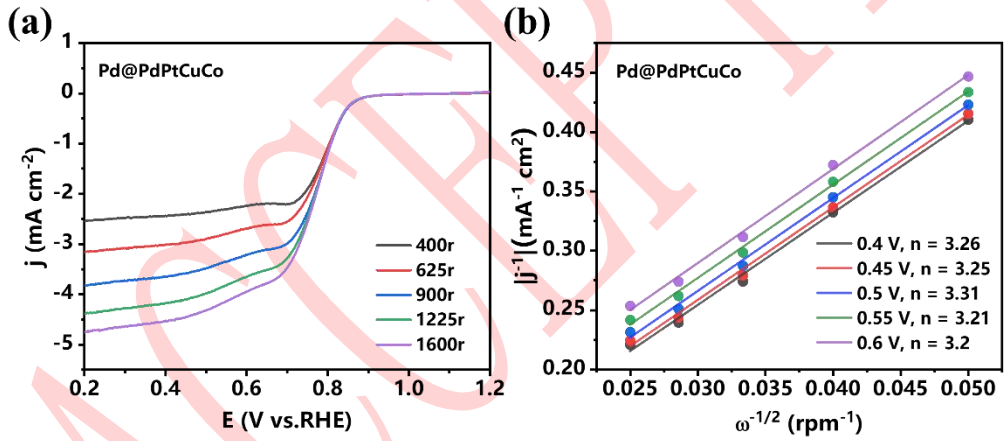

Figure S14. (a) Rotating disk voltammogram (RDV) curves at different rotation rates of Pd@PdPtCuCo in 0.1 M KOH electrolyte. (b) K−L plots.

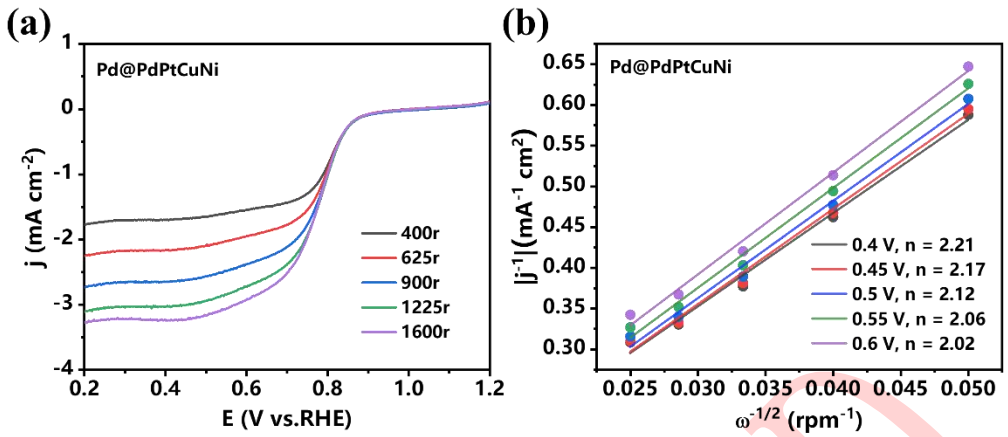

Figure S15. (a) Rotating disk voltammogram (RDV) curves at different rotation rates of Pd@PdPtCuNi in 0.1 M KOH electrolyte. (b) K−L plots.

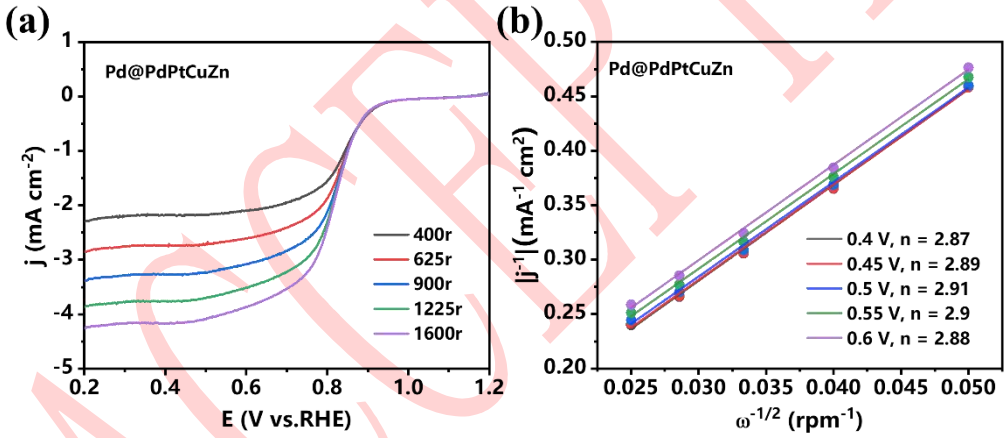

Figure S16. (a) Rotating disk voltammogram (RDV) curves at different rotation rates of Pd@PdPtCuZn in 0.1 M KOH electrolyte. (b) K−L plots.

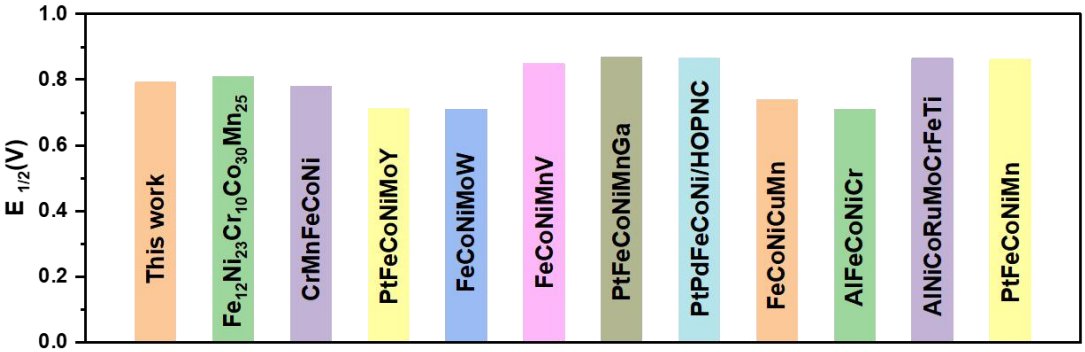

Figure S17. comparison of half-wave potentials and overpotentials with previously reported catalysts.

Table S1. The atomic ratios of Pd, Pt, Cu, and Fe in Pd@PdPtCuFe measured by EDS and the corresponding mass loadings.

Pd@PdPtCuFe	Pd	Pt	Cu	Fe
Atomic ratio (%)	55.5	35.3	8.3	1.17
Mass loading (%)	44.1	51.4	3.94	0.49

Table S2. The atomic ratios of metal components in Pd@PdPtCu and Pd@PdPtCuFe measured by XPS.

Atomic ratio (%)	Pd@PdPtCu	Pd@PdPtCuFe
Pd	24.42	15.93
Pt	49.96	57.23
Cu	25.62	16.13
Fe	/	10.71

Table S3. Double-layer capacitance and electrochemically active surface area (ECSA) of multimetallic alloy catalysts.

Sample	C_{dl} (mF cm^{-2})	ECSA (cm^2)
Pd@PdPtCu/C	1.98	49.50
Pd@PdPtCuFe/C	2.86	71.50
Pd@PdPtCuCo/C	2.07	51.75
Pd@PdPtCuNi/C	2.49	62.25
Pd@PdPtCuZn/C	2.04	51.00
Pt/C	1.73	43.25

Table S4. The HER performance of the as-prepared electrocatalysts.

Sample	HER η_{10} (mA cm^{-2})	HER Tafel slope (mV dec^{-1})
Pd@PdPtCu/C	32	34
Pd@PdPtCuFe/C	18	27
Pd@PdPtCuCo/C	22	32
Pd@PdPtCuNi/C	20	31
Pd@PdPtCuZn/C	34	44
Pt/C	27	33

Table S5. The OER performance of the as-prepared electrocatalysts.

Catalysts	OER η_{10} (mA cm^{-2})	OER Tafel slope (mV dec^{-1})
Pd@PdPtCu/C	563	156.74
Pd@PdPtCuFe/C	360	75.91
Pd@PdPtCuCo/C	450	89.79
Pd@PdPtCuNi/C	420	75.22
Pd@PdPtCuZn/C	476	132.4
IrO_2	367	77.3

Table S6. The ORR performance of the as-prepared electrocatalysts.

Catalysts	$E_{1/2}$ (V)	ORR Tafel slope (mV dec^{-1})	Average electron transfer numbers (n)
Pd@PdPtCu/C	0.752	99	3.414
Pd@PdPtCuFe/C	0.792	83	3.91
Pd@PdPtCuCo/C	0.776	91	3.246
Pd@PdPtCuNi/C	0.788	85	2.116
Pd@PdPtCuZn/C	0.765	90	2.89
Pt/C	0.825	88	3.892

Table S7. Comparison of OER performance in alkaline electrolyte between the present catalyst and reported high-entropy (multi-component) alloy catalysts.

Electrocatalysts	Electrolyte	η_{10} (mV)	Tafel slope ($mV \cdot dec^{-1}$)	Refs
Pd@PdPtCuFe	**1 M KOH**	**360**	**75.91**	**This work**
FeCoNiCuMn	1 M KOH	330	62.4	[53]
PtFeCoNiMn	1 M KOH	357	114.6	[54]
CoFeGaNiZn	1 M KOH	370	40.0	[55]
FeCoNiCuIr	1 M KOH	360	70.1	[56]
FeCoNiCuPd	1 M KOH	390	96	[57]
PtLaNiCoFe	1 M KOH	377	159	[58]
FeRuPtNiCoPd	1 M KOH	398	87	[59]
NiCoFePdIr	1 M KOH	400	134	[60]
N-PtFeNiCoMn	1 M KOH	376	/	[61]
FeCoNiPtRu	1 M KOH	331	51	[62]
CuCoNiMnAl	1 M KOH	390	65	[63]
FeCoNiCuMo	1 M KOH	324	70.5	[64]

Table S8. Comparison of ORR performance in alkaline electrolyte between the present catalyst and reported high-entropy (multi-component) alloy catalysts.

Electrocatalysts	Electrolyte	$E_{1/2}$ (V)	Refs
Pd@PdPtCuFe	**0.1 M KOH**	**0.792**	**This work**
$Fe_{12}Ni_{23}Cr_{10}Co_{30}Mn_{25}$	0.1 M KOH	0.81	[65]
CrMnFeCoNi	0.1 M KOH	0.78	[66]
PtFeCoNiMoY	0.1 M KOH	0.71	[67]
FeCoNiMoW	0.1 M KOH	0.71	[68]
FeCoNiMnV	0.1 M KOH	0.85	[69]
PtFeCoNiMnGa	0.1 M KOH	0.87	[70]
PtPdFeCoNi/HOPNC	0.1 M KOH	0.86	[71]
FeCoNiCuMn	0.1 M KOH	0.74	[53]
AlFeCoNiCr	0.1 M KOH	0.71	[72]
AlNiCoRuMoCrFeTi	0.1 M KOH	0.86	[73]
PtFeCoNiMn	0.1 M KOH	0.86	[54]

References

(53) Tanmathusorachai W, Aulia S, Rinawati M, Chang L Y, Chang C Y, Huang W H, Lin M H, Su W N, Yuliarto B, Yeh M H. High-entropy prussian blue analogue derived heterostructure nanoparticles as bifunctional oxygen conversion electrocatalysts for the rechargeable zinc-air battery[J]. ACS Appl. Mater. Interfaces 2024, 16(45): 62022-62032. http://dx.doi.org/10.1021/acsami.4c13387

(54) Xie M K, Xiao X, Wu D J, Zhen C, Wu C S, Wang W J, Nian H, Li F Y, Gu M D, Xu Q. MOF-mediated synthesis of novel PtFeCoNiMn high-entropy nano-alloy as bifunctional oxygen electrocatalysts for zinc-air battery[J]. Nano Res., 2024, 17(6): 5288-5297. http://dx.doi.org/10.1007/s12274-024-6526-4

(55) Sharma L, Katiyar N K, Parui A, Das R, Kumar R, Tiwary C S, Singh A K, Halder A, Biswas K. Low-cost high entropy alloy (HER) for high-efficiency oxygen evolution reaction (OER)[J]. Nano Res., 2022, 15(6): 4799-4806. http://dx.doi.org/10.1007/s12274-021-3802-4

(56) Zhao M, Elnabawy A O, Vara M, Xu L, Hood Z D, Yang X, Gilroy K D, Figueroa-Cosme L, Chi M F, Marvrikakis M, Xia Y N. Facile synthesis of Ru-based octahedral nanocages with ultrathin walls in a face-centered cubic structure[J]. Chem Mater, 2017, 29(21): 9227-9237. http://dx.doi.org/10.1021/acs.chemmater.7b03092

(57) Li H N, Zhu H, Shen Q K, Huang S D, Lu S L, Ma P M, Dong W F, Du M L. A novel synergistic confinement strategy for controlled synthesis of high-entropy alloy electrocatalysts[J]. Chem. Commun., 2021, 57(21): 2637-2640. http://dx.doi.org/10.1039/d0cc07345h

(58) Glasscott M W, Pendergast A D, Goines S, Bishop A R, Hoang A T, Renault C, Dick J E. Electrosynthesis of high-entropy metallic glass nanoparticles for designer, multi-functional electrocatalysis[J]. Nat Commun, 2019, 10: http://dx.doi.org/10.1038/s41467-019-10303-z

(59) Lee Y, Theerthagiri J, Limphirat W, Periyasamy G, Jeong G H, Kheawhom S, Tang Y B, Choi M Y. Pulsed laser-patterned high-entropy single-atomic sites and alloy coordinated graphene oxide for pH-universal water electrolysis[J]. J Mater Chem A, 2025, 13: 9073-9087. http://dx.doi.org/10.1039/d5ta00117j

(60) Sarsenov S, Moon C J, Senthil R A, Kumar A, Maheskumar V, Ubaidullah M, Kanjanapaparkul K, Kheawhom S, Choi M Y. Harnessing the surface-stabilized high-entropy alloy and nitrogen-doped carbon interplay for superior Zn-air battery performance[J]. Energy Storage Mater, 2025, 81: 104507. http://dx.doi.org/10.1016/j.ensm.2025.104507

(61) Niu M, Guan Q H, Yuan W Y, Guo C X, Cao D P, Li C M, Zhang L Y, Zhao X S. Significantly improving the stability of high-entropy PtFeNiCoMn nanoalloys by nitrogen doping in oxygen electrocatalysis[J]. Chem. Eng. J., 2025, 503: 158465. http://dx.doi.org/10.1016/j.cej.2024.158465

(62) Geng M M, Zhu Y J, Guan J B, Zhang R, Zou Q, Wang L N, Guo B C, Zhang M. Carbothermal shock synthesis of FeCoNiPtRu high-entropy alloy for dual-function water splitting in alkaline media[J]. J. Alloys Compd., 2024, 1005: 176180. http://dx.doi.org/10.1016/j.jallcom.2024.176180

(63) Zhu X Q, Li J, Ali R N, Song M. Two-dimensional ultra-thin cuconimnal high-entropy alloy nanosheets for lithium-ion storage and oxygen evolution reaction[J]. J. Power Sources, 2024, 610: http://dx.doi.org/10.1016/j.jpowsour.2024.234738
(64) Ma J T, Zhu Y J, Huang K, Wang P, Liu D H, Zhao Y P. High-entropy alloy catalysts of FeCoNiCuMo/C with high stability for efficient oxygen evolution reaction[J]. J. Alloys Compd., 2024, 997: 174922. http://dx.doi.org/10.1016/j.jallcom.2024.174922
(65) Cao X H, Gao Y T, Wang Z H, Zeng H Z, Song Y F, Tang S G, Luo L X, Gong S. FeNiCrCoMn high-entropy alloy nanoparticles loaded on carbon nanotubes as bifunctional oxygen catalysts for rechargeable zinc-air batteries[J]. ACS Appl. Mater. Interfaces 2023, 15(27): 32365-32375. http://dx.doi.org/10.1021/acsami.3c04120
(66) He R, Yang L L, Zhang Y, Wang X, Lee S, Zhang T, Li L X, Liang Z F, Chen J W, Li J S, Moghaddam A O, Llorca J, Ib M, Arbiol J, Xu Y, Cabot A. A CrMnFeCoNi high entropy alloy boosting oxygen evolution/reduction reactions and zinc-air battery performance[J]. Energy Storage Mater, 2023, 58: 287-298. http://dx.doi.org/10.1016/j.ensm.2023.03.022
(67) Han J L, Zhang W X, Liu K Z, Zheng H J, Li Y M, Luo L X, Gong S, Jia Y L, Liang X P. PtFeCoNiMoY high-entropy alloy nanoparticles as bifunctional oxygen catalysts for zinc air batteries[J]. Appl. Surf. Sci., 2025, 687: 162238. http://dx.doi.org/10.1016/j.apsusc.2024.162238
(68) He R, Yang L L, Zhang Y, Jiang D, Lee S, Horta S, Liang Z F, Lu X, Moghaddam A O, Li J S, Ibáñez M, Xu Y, Zhou Y T, Cabot A. A 3d-4d-5d high entropy alloy as a bifunctional oxygen catalyst for robust aqueous zinc-air batteries[J]. Adv. Mater., 2023, 35(46): 2303719. http://dx.doi.org/10.1002/adma.202303719
(69) Wu D H, Ul Haq M, Zhang L, Feng J J, Yang F, Wang A J. Noble metal-free feconimnv high entropy alloy anchored on N-doped carbon nanotubes with prominent activity and durability for oxygen reduction and zinc-air batteries[J]. J. Colloid Interface Sci., 2024, 662: 149-159. http://dx.doi.org/10.1016/j.jcis.2024.02.044
(70) Luo L X, Tang R X, Su L, Kou J Y, Guo X, Li Y K, Cao X H, Cui J Y, Gong S. Data-driven designed low pt loading PtFeCoNiMnGa nano high entropy alloy with high catalytic activity for Zn-air batteries[J]. Energy Storage Mater, 2024, 72: 103773. http://dx.doi.org/10.1016/j.ensm.2024.103773
(71) Xie M K, Lu Y, Xiao X, Wu D J, Shao B, Nian H, Wu C S, Wang W J, Gu J, Han S B, Gu M, Xu Q. Spatially immobilized PtPdFeCoNi as an excellent bifunctional oxygen electrocatalyst for zinc-air battery[J]. Adv. Funct. Mater., 2025, 35(5): 2414537. http://dx.doi.org/10.1002/adfm.202414537
(72) Fang G, Gao J J, Lv J, Jia H L, Li H L, Liu W H, Xie G Q, Chen Z H, Huang Y, Yuan Q H, Liu X J, Lin X, Sun S H, Qiu H J. Multi-component nanoporous alloy/(oxy)hydroxide for bifunctional oxygen electrocatalysis and rechargeable Zn-air batteries[J]. Appl Catal B Environ, 2020, 268: 11843. http://dx.doi.org/10.1016/j.apcatb.2019.118431
(73) Jin Z Y, Lyu J, Hu K L, Chen Z H, Xie G Q, Liu X J, Lin X, Qiu H J. Eight-component nanoporous high-entropy oxides with low Ru contents as high-performance bifunctional catalysts in Zn-air batteries[J]. Small, 2022, 18(12): 2107207. http://dx.doi.org/10.1002/smll.202107207